Journal of Advanced Ceramics
2024, **13**(1): 86–100
https://doi.org/10.26599/JAC.2024.9220838

Research Article

Toughened $(Ti_{0.2}Zr_{0.2}Hf_{0.2}Nb_{0.2}Ta_{0.2})B_2$–SiC composites fabricated by one-step reactive sintering with a unique SiB_6 additive

Wei Hao[1,✉], Xinzhe Lu[1], Ling Li[3], Tao Wang[1], Guoliang Ren[3], Huangyue Cai[3], Xiaofeng Zhao[3], Dongyun Wang[1], Na Ni[2,✉]

[1] *Zhejiang Provincial Key Laboratory of Urban Rail Transit Intelligent Operation and Maintenance Technology & Equipment, Zhejiang Normal University, Zhejiang 321004, China*
[2] *Key Lab of Education Ministry for Power Machinery and Engineering, School of Mechanical Engineering, Shanghai Jiao Tong University, Shanghai 200240, China*
[3] *School of Materials Science and Engineering, Shanghai Jiao Tong University, Shanghai 200240, China*

Received: July 9, 2023; Revised: December 3, 2023; Accepted: December 6, 2023

Abstract: High-entropy diboride has been arousing considerable interest in recent years. However, the low toughness and damage tolerance limit its applications as ultra-high-temperature structural materials. Here we report that a unique SiB_6 additive has been first incorporated as boron and silicon sources to fabricate a high-entropy boride $(Ti_{0.2}Zr_{0.2}Hf_{0.2}Nb_{0.2}Ta_{0.2})B_2$–SiC composite though one-step boro/carbothermal reduction reactive sintering. A synergetic effect of high-entropy sluggish diffusion and SiC secondary phase retarded the grain growth of the $(Ti_{0.2}Zr_{0.2}Hf_{0.2}Nb_{0.2}Ta_{0.2})B_2$–51SiC composites. The small grain size was beneficial to shorten the diffusion path for mass transport, thereby enhancing the relative density to ~99.3%. These results in an increase of fracture toughness from ~5.2 in HEBS-1900 to ~7.7 MPa·m$^{1/2}$ in HEBS-2000, which corresponded to a large improvement of 48%. The improvement was attributed to a mixed mode of intergranular and transgranular cracking for offering effective pinning in crack propagation, resulting from balanced grain boundary strength collectively affected by improved densification, solid solution strengthening, and incorporation of SiC secondary phase.

Keywords: high-entropy diboride; silicon hexaboride; boro/carbothermal reduction; reactive sintering; fracture toughness

1 Introduction

High-entropy diboride (HEB) is important ultra-high temperature ceramics that possess many desired performances such as high Young's modulus, strength, and hardness, excellent high-temperature stability, and superior oxidation resistance [1–3]. Significantly, HEB ceramics possess enormous potential for broad applications owing to their huge composition space, unique microstructure, and adjustable properties [4–6]. However, Achilles' heel of HEB ceramics is their relatively low toughness (2.8–4.1 MPa·m$^{1/2}$), which can limit their applications as ultra-high-temperature structural materials in extreme environments [1,7–9].

To overcome this problem, the transitional metals (Hf, Zr, and Cr) were incorporated into HEB to toughen HEB–Hf, HEB–Zr, and HEB–Cr composites and improve K_{IC} up to ~9.2, ~7.1, and ~7.3 MPa·m$^{1/2}$, respectively [10]. Although the addition of Hf, Zr, and Cr contributed to a large toughening effect for HEB ceramics, the phase transformation of Hf metal additive easily occurred from hexagonal close-packed structure to body-centered cubic structure at ~1757 ℃ [11], and the Cr addition can react with diborides and SiC to produce liquid phases at high temperature to form new solid phases [12]. Notably, the ductile nature of Zr phase addition decreased the hardness and high-temperature mechanical properties of diboride–Zr ceramics [13]. These issues were detrimental to high-temperature stability and mechanical properties of HEB-based ceramics. On the other hand, incorporating a secondary component in HEB ceramics is an effective approach. Consequently, dual-phase high-entropy ceramics were fabricated to increase the fracture toughness from 2.3 to 4.7 MPa·m$^{1/2}$ in $(Ti_{0.2}Zr_{0.2}Hf_{0.2}Nb_{0.2}Ta_{0.2})B_2$–$(Ti_{0.2}Zr_{0.2}Hf_{0.2}Nb_{0.2}Ta_{0.2})C$ through the boro/carbothermal reduction (BCTR) approach due to the enhanced densification and smaller grain size (~1.5 μm) [14,15].

In terms of the choice of secondary phases, SiC not only possesses an obvious strengthening effect but also improves the fracture toughness from ~3.8 MPa·m$^{1/2}$ for HEB without SiC addition to ~4.9 MPa·m$^{1/2}$ for HEB containing 20 vol% SiC addition, showing a great improvement of 29% [8]. In another high entropy boride system, Jin *et al.* [16] reported that K_{IC} was improved from 3.1 to 4.9 MPa·m$^{1/2}$ with the addition of 15 wt% SiC into single-phase $(Ti_{0.2}Hf_{0.2}Nb_{0.2}Ta_{0.2}Mo_{0.2})B_2$. It can be found that the addition of SiC secondary particles can inhibit the grain growth and improve the densification, hardness, and fracture toughness of high-entropy ceramics, which were attributed to fine-grained microstructure, lattice distortion, and crack deflection [8,16–18]. Besides, the incorporation of SiC into HEB ceramics can improve their oxidation resistance of HEB-based ceramics [19]. However, the above research has been focused on the simple sintering of the pre-synthesized HEB and SiC powder mixture through spark plasma sintering (SPS) or hot pressing method

✉ Corresponding authors.
E-mail: W. Hao, haoweimaster@163.com;
N. Ni, na.ni@sjtu.edu.cn

[4,8], where the final microstructure is largely determined by the pre-defined powder chemistry and morphology before the sintering process.

To design pre-defined HEB-based powder composition and morphology for fabricating composites with desired microstructures, some powder synthesis methods were used to controllably fabricate HEB powders, such as self-propagating high-temperature synthesis [20], borothermal reduction (BTR) [21], molten salt-mediated magnesiothermic reduction [22], sol–gel method [23], BCTR [24], The first four methods easily introduced oxide impurities and unreacted B in the as-synthesized HEB powders [20–23]. The existence of oxide impurities and unreacted B suppressed the densification of HEB ceramics [25], and resulted in the reduction of high-temperature mechanical properties of HEB-based ceramics [13]. The BCTR method has been considered as a facile route to fabricate diborides, HEB powders, and bulk materials without oxide impurities [24,26,27]. B_4C, boron, and nano-carbon powders were mostly used as boron and carbon sources in the previous work, respectively [25,26,28]. Gong *et al.* [29] reported that (V,Ti,Ta,Nb)B_2–SiC powders were synthesized using transitional metal oxides, Si, carbon black, and B_4C as raw materials through high-energy ball milling-assisted BCTR, which mainly investigated the synthesis of (V,Ti,Ta,Nb)B_2–SiC powders and their electromagnetic wave absorbing properties. However, previous studies focused mainly on the synthesis of single-phase HEB and HEB–SiC powders, while the design and synthesis of HEB–SiC composite powders were rarely reported for tailoring the final microstructure of bulk materials to toughening HEB ceramics. We have previously reported the fabrication of HfC–HfB_2 composites through reactive sintering using silicon hexaboride (SiB_6) as a novel sintering additive and found that the reactive sintering nature was beneficial to the *in-situ* formation of HfB_2, promoting the composites densification [30,31].

Nevertheless, the feasibility of using SiB_6 as boron and silicon sources to synthesize HEB–SiC composite powders and bulk materials has not been explored, and the exact role of SiB_6 in the formation of HEB and SiC and the densification of the bulk materials needs to be clarified. Therefore, this work aims to extend the use of SiB_6 as the unique boron and silicon source to fabricate uniform and dense HEB–SiC composites through one-step BCTR reactive sintering. $(Ti_{0.2}Zr_{0.2}Hf_{0.2}Nb_{0.2}Ta_{0.2})B_2$–SiC composite powders and bulk materials were both prepared and the microstructural evolution, densification, and fracture toughness were investigated. The underlying mechanisms for the chemical reaction thermodynamics, improved density, and fracture toughness were also discussed.

2 Experimental

2.1 Hot pressing sintering

The powders of HfO_2, ZrO_2, Ta_2O_5, Nb_2O_5, TiO_2 (purity ≥ 99.95%, mean particle size of 100 nm, Shanghai Chao Wei Nano Technology Co., Ltd, China), SiB_6 (purity of 98%, main impurity includes Si < 2%, particle size of 3–8 μm, Shanghai Alfa Aesar Co., Ltd, China), and nano-carbon black (purity ≥ 99.9%, particle size of 50 nm, Beijing InnoChem Science & Technology Co., Ltd, China) were utilized as starting materials. The powders were mixed as follows: 6 mol% HfO_2, 6 mol% ZrO_2, 3 mol% Ta_2O_5, 3 mol% Nb_2O_5, 6 mol% TiO_2, 10 mol% SiB_6, and 76 mol% nano-carbon black, and ball-milled with SiC balls for 12 h using isopropanol as a milling medium. After drying at 60 ℃ for 2 h, the mixture of the above powders was put into a graphite crucible with a graphite foil, and the whole assembly was placed into a vacuum furnace (ZT-63-20Y, Shanghai ChenHua Electric Furnace Co., Ltd., China). The system was heated from room temperature to 1900 and 2000 ℃ at a rate of 10 ℃/min. Then, it was maintained for 2 or 4 h in a vacuum (10^{-2} Pa) for BCTR, and finally cooled down to room temperature. The as-prepared powders are named HEB2-1900 (BCTR at 1900 ℃ for 2 h), HEB2-2000 (BCTR at 2000 ℃ for 2 h), and HEB4-2000 (BCTR at 2000 ℃ for 4 h).

Bulk composite samples were also reactively sintered by hot-pressing sintering technique in a furnace under a vacuum (10^{-2} Pa). The mixture of the above raw powders was prepared in the same way as described above and put into a 31 mm graphite die, which was lined with 0.3 mm thick graphite foils to maximize the thermal conduction between the punches and the die. The whole assembly was heated from room temperature to 1900 and 2000 ℃ at a rate of 10 ℃/min for BCTR reactive sintering. After dwell time of 2 or 4 h at 30 MPa, the applied pressure was immediately reduced to the initial pressure of 6.6 MPa, and the furnace was naturally cooled to room temperature. The bulk composite samples fabricated at 1900 and 2000 ℃ are named HEBS-1900 and HEBS-2000, respectively.

2.2 Characterization of as-sintered high-entropy diboride composites

2.2.1 *Structure characterization*

The phase composition of the as-sintered powders and composites was analyzed by an X-ray diffractometer (XRD; Ultima IV, Rigaku, Japan). The microstructure and chemical composition of the BCTR powders and reactive sintered composites were characterized by a field emission scanning electron microscope (FE-SEM; MIRA3-LHM 5–20 kV, TESCAN, Czech) equipped with an energy dispersive X-ray spectroscope (EDX; Aztec X-MaxN80 20 kV, Oxford Instruments, UK), and a scanning transmission electron microscope ((S)TEM, TALOS F200 X 200 kV, Thermo Fisher, USA) equipped with an energy dispersive X-ray spectroscope (EDX; Super-X 200 kV, Thermo Fisher, USA). TEM specimens of selected sintered samples were prepared using a focused ion beam (SEM-FIB; GAIA3 GMU, TESCAN, Czech). The particle sizes of as-synthesized powders were evaluated using a laser diffraction spectrometer (LDS; S3500, MICROTRAC, USA). The true density of the bulk samples was measured using Archimedes' method in distilled water. The grain size was evaluated and calculated for both the BCTR powders and reactive sintered composites using the linear method on at least 500 grains. A quantitative assessment was used to estimate the phase fraction in powder and bulk samples by combining XRD Rietveld refinement using the Maud software [32] and image analysis (Image J, 1.52a, National Institutes of Health, USA) based on 10 STEM high-angle annular dark field (HAADF) images of powder or bulk samples. The low related fitting parameter values for XRD Rietveld refinement were R_{wp} = 8.72% and χ^2 = 1.925 for HEB2-1900, R_{wp} = 9.29% and χ^2 = 2.052 for HEB2-2000, R_{wp} = 6.75% and χ^2 = 1.543 for HEBS-1900, and R_{wp} = 8.76% and χ^2 = 1.895 for HEBS-2000 where R_{wp} is the weighted pattern variance factor, and χ^2 is the goodness of fit . The oxygen content within the bulk samples was analyzed by an element analyzer (ELEMENTRAC ONH-P, Eltra GmbH, Germany).

2.2.2 *Mechanical tests*

Mechanical properties of the as-sintered composites were measured by indentation tests using a micro indentation tester

(Anton Paar, CPX MHT, Austria) with a diamond Vickers indenter. The Young's modulus (E) and Vickers hardness (H) of the ceramic sample were estimated from the load–displacement curves. A total of 20 indentations with 60 μm intervals were made using a load of 1 N with dwell time of 10 s. For fracture toughness measurements, indentation tests were also performed at different loads (5, 10, 15, 20, and 25 N) on the well-polished surface of the bulk ceramic samples to induce radial cracking from the corners of the indentation. The length of the radial cracks were then measured from the center of the indention using SEM. A total of 20 indentations were conducted on each sample. A semi-empirical fracture mechanics analysis of the cracks associated with Vickers indentations yields a measure of toughness.

3 Results

3.1 Structure of as-synthesized (Ti,Zr,Hf,Nb,Ta)B_2–SiC powders

Figure 1(a) shows XRD patterns of the as-synthesized (Ti,Zr,Hf,Nb,Ta)B_2–SiC powders through BCTR under different conditions. Two sets of diffraction peaks for phases with the AlB_2 structure were detected after heating to 1900 and 2000 ℃ for 2 h. The as-prepared composite powders are composed of a dominant(Ti,Zr,Hf,Nb,Ta)B_2 phase and two minor (Zr,Hf)B_2 and hexagonal SiC phases (HEB2-1900 and HEB2-2000) (Fig. 1), indicating that the solid solution reactions between raw materials were not complete at 1900 ℃ for short holding time. This trend has been investigated in the previous studies [21,26]. Moreover, no diffraction peaks of oxides were detected by XRD analysis, which is likely attributed to the BCTR reactions for the removal of oxides impurities [24,27]. With the increase of the reactive temperature and holding time, the diffraction peak intensity ratios ($I_{(101)\,HEB}/I_{(101)\,(Zr,Hf)B_2}$) of their (101) crystal planes for (Ti,Zr,Hf,Nb,Ta)B_2 and (Zr,Hf)B_2 phases were calculated to be 1.14 for HEB2-1900, 1.25 for HEB2-2000, and 1.29 for HEB4-2000 (Fig. 1(b)). This suggests that the relative diffraction peaks intensity of the (Ti,Zr,Hf,Nb,Ta)B_2 phase gradually increases, but that of binary solid solution (Zr,Hf)B_2 declines in the (Ti,Zr,Hf,Nb,Ta)B_2–SiC powders.

Figures 2(a) and 2(b) present SEM-EDX elemental mapping analyses of the HEB2-1900 and HEB2-2000 powders, respectively. The Zr, Nb, and Ti segregation in the scanned microscale area

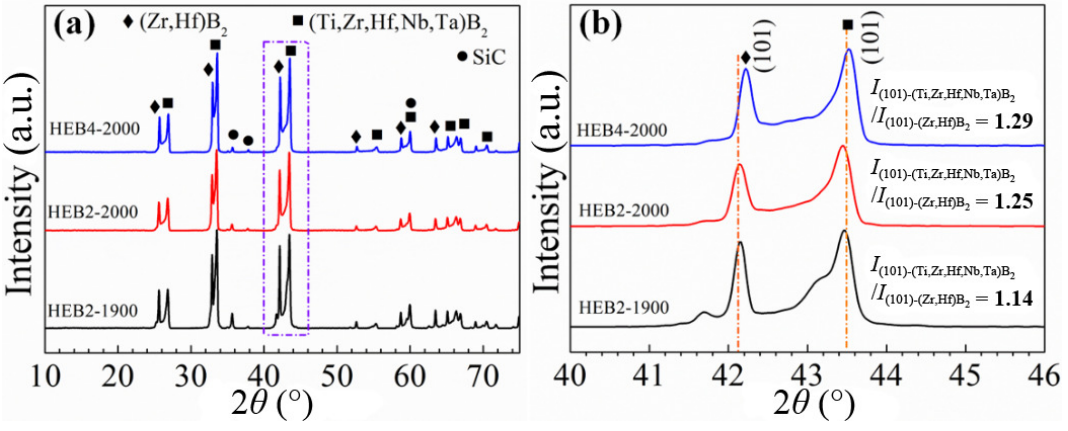

Fig. 1 (a) XRD patterns and (b) local magnification at 2θ range of 40°–46°of as-synthesized (Ti,Zr,Hf,Nb,Ta)B_2–SiC powders through BCTR with SiB_6 additive.

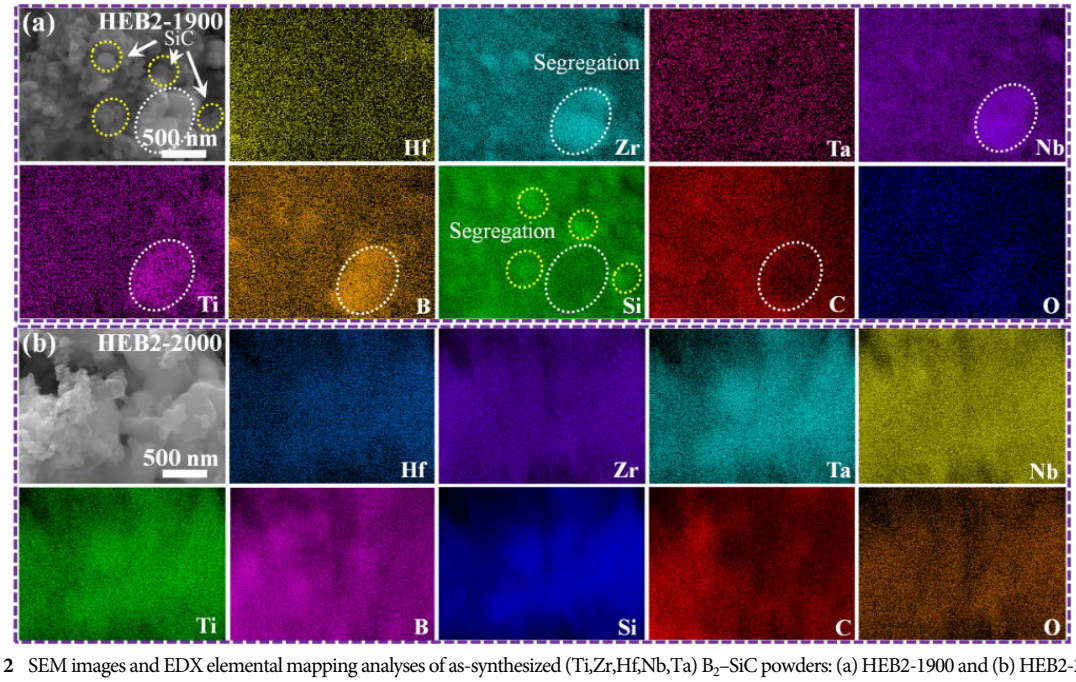

Fig. 2 SEM images and EDX elemental mapping analyses of as-synthesized (Ti,Zr,Hf,Nb,Ta) B_2–SiC powders: (a) HEB2-1900 and (b) HEB2-2000.

were detected in the HEB2-1900 sample (Fig. 2(a)), which demonstrated that the above elements could not be completely dissolved into the (Ti,Zr,Hf,Nb,Ta)B_2 phase during the solid solution reaction. The Si-enriched areas may be assigned to the SiC particles. Figures 3(a) and 3(b) show STEM BF and HAADF images of HEB2-1900 powders. Together with the STEM-EDX mapping analyses (Fig. 3(c)), it can be confirmed that the bright particles in the *Z* contrast-dominated STEM HAADF image contain mainly Ti, Zr, Hf, Nb, Ta, and B, and the gray particles contain only Zr, Hf, and B in the scanned nanoscale areas, which correspond to the formed (Ti,Zr,Hf,Nb,Ta)B_2 and (Zr,Hf)B_2, respectively. Closer investigation reveals that the SiC particles with dark contrast were observed in HEB2-1900 powders. Notably, for the HEB2-2000 sample, a homogeneous distribution of Hf, Zr, Ta, Nb, Ti, and Si was detected in the scanned microscale area, and no segregation or aggregation was found (Fig. 2(b)), which implied that the as-synthesized HEB2-2000 powders possessed more compositional uniformity at the micrometer scale. Furthermore, STEM BF (Fig. 3(d)) and HAADF images (Fig. 3(e)), and STEM-EDX mapping analyses (Fig. 3(j)) revealed that the HEB2-2000 powders also contain (Ti,Zr,Hf,Nb,Ta)B_2, (Zr,Hf)B_2, and SiC phases. A homogeneous distribution of Hf, Zr, Ta, Nb, Ti, and Si for the (Ti,Zr,Hf,Nb,Ta)B_2 grains was detected in the nanoscale scanned areas, but Hf and Zr elements were enriched in the minor (Zr,Hf)B_2 grains. The HRTEM images of (Ti,Zr,Hf,Nb,Ta)B_2 and (Zr,Hf)B_2 phases show periodic lattice structures with two sets of lattice fringes with *d*-space of 0.33 nm (Figs. 3(g) and 3(i), the area I in Fig. 3(f)) and 0.35 nm (Fig. 3(h), the area II in Fig. 3(f)), respectively, corresponding to the {001} lattice spacings of hexagonal diborides. The grain boundary between (Ti,Zr,Hf,Nb,Ta) B_2 and SiC grains was also observed in HRTEM (Fig. 3(i), the area III in Fig. 3(f)), and a set of lattice fringes with *d*-space of 0.25 nm corresponds to the (001) crystal plane of the hexagonal SiC phase (PDF No. 51-0639) (Fig. 3(i)). These are consistent with XRD results. Figure 4 shows STEM images and STEM-EDX mapping analyses of the HEB4-2000 powders. Consistent with the XRD results, it was found that the phase composition of the samples is similar to those of HEB2-2000 powders; however the content of binary solid solution (Zr,Hf)B_2 decreased in the HEB4-2000 powders (Figs. 4(b) and 4(c)).

The phase composition of the (Ti,Zr,Hf,Nb,Ta)B_2–SiC powders is summarized in Table 1. The contents of the (Ti,Zr,Hf,Nb,Ta)B_2

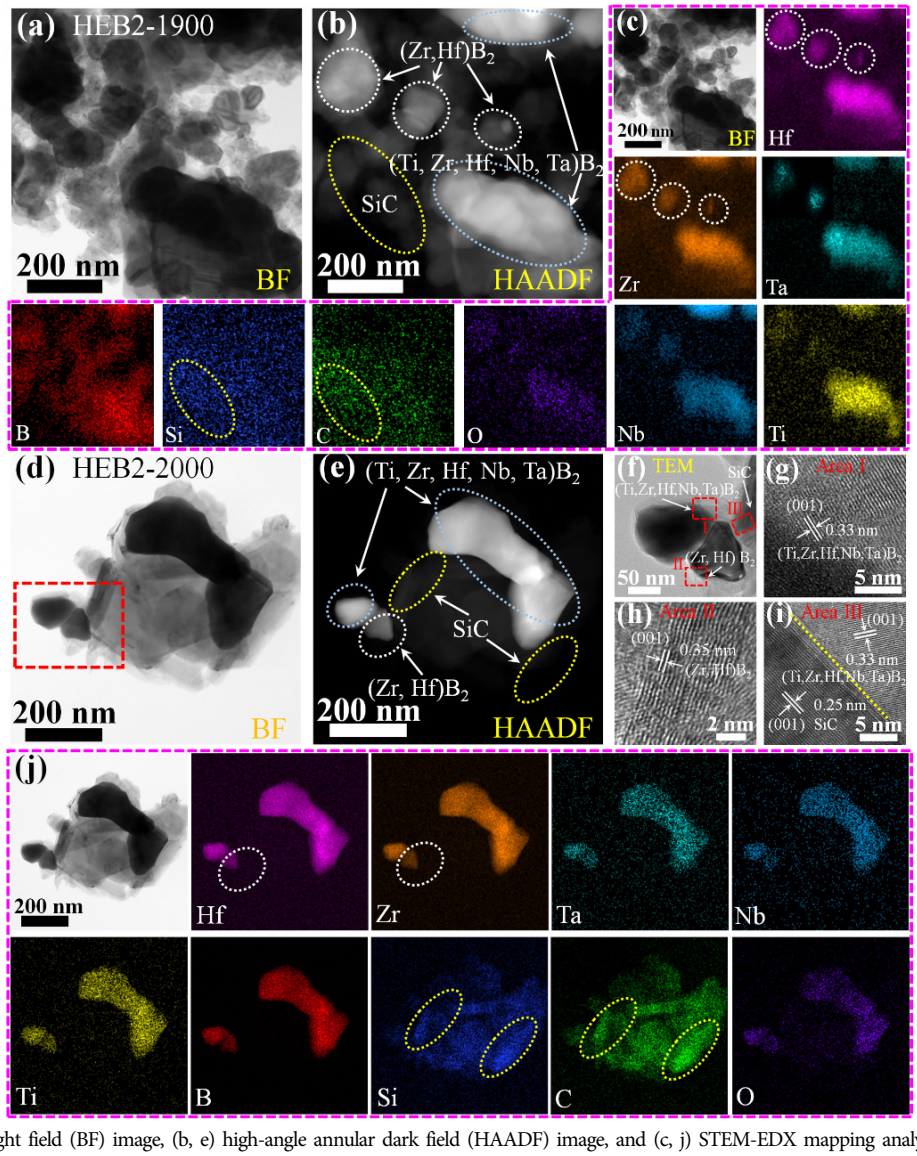

Fig. 3 (a, d) STEM bright field (BF) image, (b, e) high-angle annular dark field (HAADF) image, and (c, j) STEM-EDX mapping analyses of (a–c) HEB2-1900 and (d, e, j) HEB2-2000 powders. (f) TEM image. HRTEM images: (g) area I in (f); (h) area II in (f); (i) area III in (f) of HEB2-2000 powders.

清華大学出版社 Tsinghua University Press | SciOpen

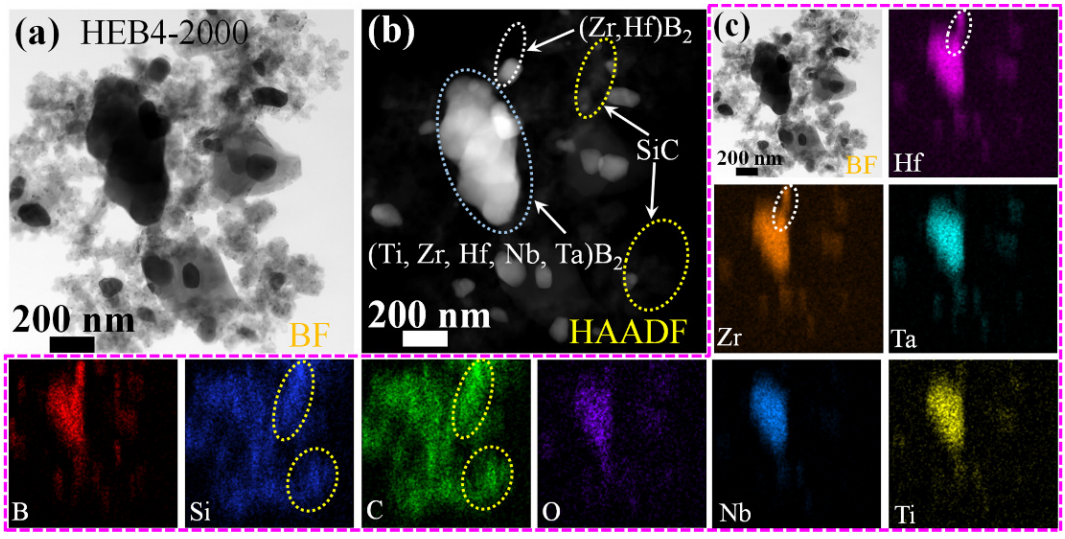

Fig. 4 (a) STEM BF image, (b) HAADF image, and (c) STEM-EDX mapping analyses of HEB4-2000 powders.

phase increased with the increase of the reactive temperature and holding time. The formed $(Zr,Hf)B_2$ phase content decreased from 20.1 wt% in HEB2-1900 to 14.3 wt% in HEB2-2000 powders (Table 1). STEM-EDX analyses of $(Ti,Zr,Hf,Nb,Ta)B_2$–SiC powders were performed to analyze the oxygen content, and the oxygen contents of three powder samples were 0.51 at% O (0.06 wt% O) (Figs. 5(a) and 5(d)) for HEB2-1900, 0.26 at% O (0.04 wt% O) (Figs. 5(b) and 5(e)) for HEB2-2000, and 0.70 at% O (0.08 wt% O) (Figs. 5(c) and 5(f)) for HEB4-2000, which were lower than those of the HEB powders synthesized by the sol–gel method (~4.0 at% O) [23] and boro/carbothermal reduction (~0.3 wt% O) [25] reported in the previous work.

Figure 6 shows SEM images of the HEB2-1900, HEB2-2000, and HEB4-2000 powders. Loose agglomerates of diboride solid solution and SiC particles were formed after BCTR at 1900 ℃ for 2 h (Figs. 6(a) and 6(d)), and the particle size of HEB2-1900 powders was in the range of 0.2–20 μm with an average value of 8.0±0.2 μm, as seen in Fig. 6(g). Notably, fine and homogeneously intermixed particles were observed in the HEB2-2000 powders (Fig. 6(b)), although slight agglomerates of more than 500 nm in diameter were also found for the HEB2-2000 sample (Fig. 6(e)). It is consistent with STEM HAADF observations that the 500 nm

Table 1 Phase compositions of as-prepared $(Ti,Zr,Hf,Nb,Ta)B_2$–SiC powders characterized by STEM-EDX analyses

Composite powder sample	Phase composition (wt%)		
	$(Ti,Zr,Hf,Nb,Ta)B_2$	$(Zr,Hf)B_2$	SiC
HEB2-1900	43.6	20.1	36.3
HEB2-2000	47.5	14.3	38.2
HEB4-2000	48.6	12.8	38.6

nanoparticle clusters can be formed in HEB2-2000 powders, and the average particle size of them was 8.2±0.2 μm. BCTR should be promoted by particle size reduction and intermixing due to the reduction in diffusion distance between the reactants [24,25]. With the increase of the reactive temperature and holding time, severe agglomerates of $(Ti,Zr,Hf,Nb,Ta)B_2$, $(Zr,Hf)B_2$, and SiC particles were formed in the HEB4-2000 powders (Fig. 6(c)). The formation of necks between particles indicates that sintering occurred during BCTR due to the presence of intermediate liquid B_2O_3 [25], which was attributed that the atoms near the boundary of each particle migrated together and formed necking to minimize the surface energy at high temperatures [33,34].

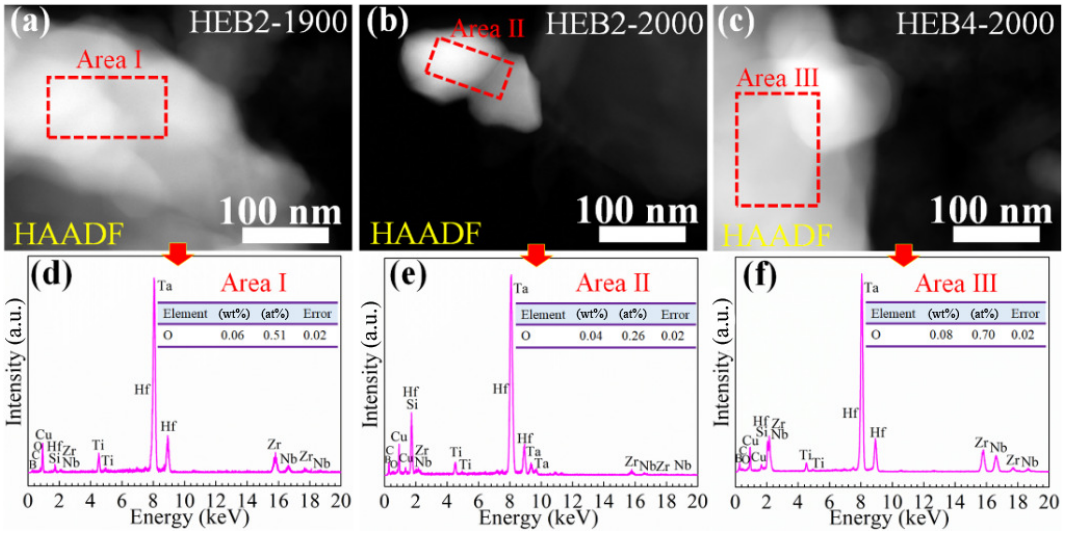

Fig. 5 (a–c) STEM HAADF images and (d–f) STEM-EDX area analyses of (a, d) HEB2-1900, (b, e) HEB2-2000, and (c, f) HEB4-2000 powders.

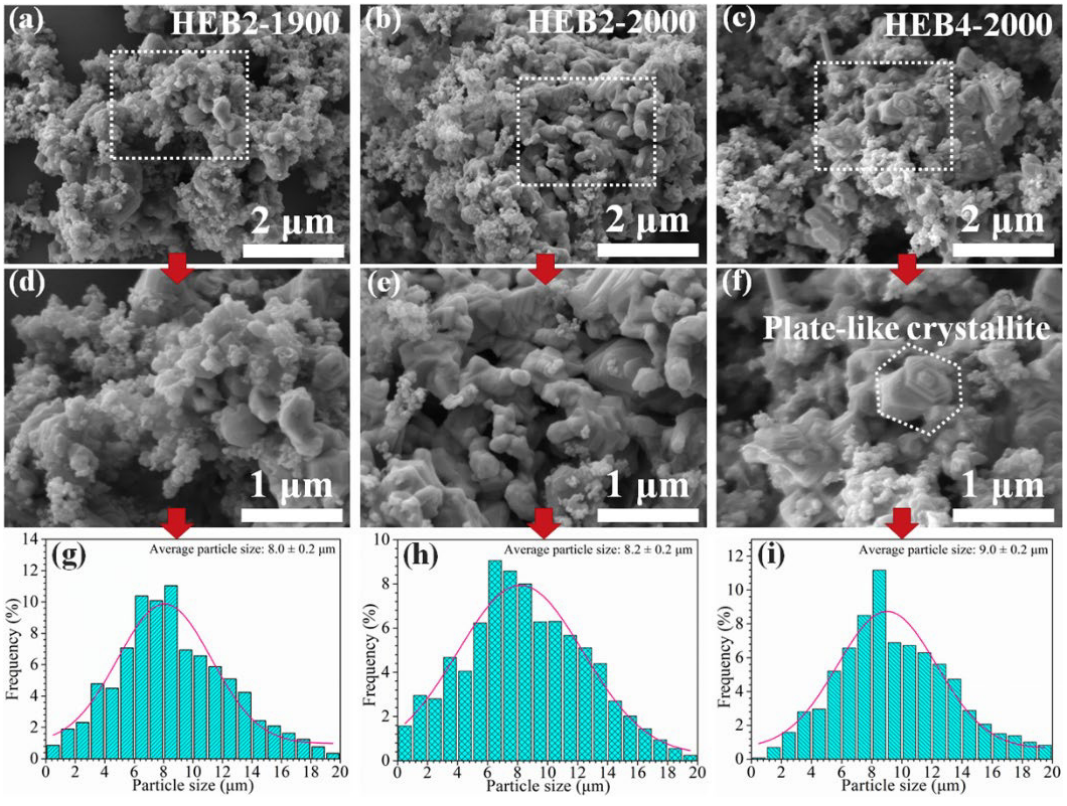

Fig. 6 (a–f) SEM images and histogram of particle sizes with Gaussian fitting to (g–i) data of as-synthesized (Ti,Zr,Hf,Nb,Ta)B_2–SiC powders: (a, d, g) HEB2-1900; (b, e, h) HEB2-2000; (c, f, i) HEB4-2000. Gaussian peaks of them are centered at 8.0±0.2 μm (HEB2-1900), 8.2±0.2 μm (HEB2-2000), and 9.0±0.2 μm (HEB4-2000).

Significant grain growth of (Ti,Zr,Hf,Nb,Ta)B_2 and SiC particles is observed in this sample. The average particle size increases from 8.0±0.2 μm for HEB2-1900 (Fig. 6(g)) to 9.0±0.2 μm for HEB4-2000 (Fig. 6(i)). Sintering of particles is promoted due to the high temperature and material transport required for solid solution formation, resulting in the formation of hexagonal plate-like (Ti,Zr,Hf,Nb,Ta)B_2 crystallites (Fig. 6(f)).

3.2 Structure of as-sintered $(Ti_{0.2}Zr_{0.2}Hf_{0.2}Nb_{0.2}Ta_{0.2})B_2$–SiC composites

XRD patterns of the HEBS-1900 and HEBS-2000 composites sintered at different temperatures are shown in Fig. 7. The HEBS-1900 composite exhibits a two-phase composition of a dominant $(Ti_{0.2}Zr_{0.2}Hf_{0.2}Nb_{0.2}Ta_{0.2})B_2$ (HEB) and minor SiC phases without (Zr,Hf)B_2 phase. Sharp diffraction peaks of HEB and SiC phases appear, which suggests that a $(Ti_{0.2}Zr_{0.2}Hf_{0.2}Nb_{0.2}Ta_{0.2})B_2$–SiC composite has been successfully produced through one-step BCTR reactive sintering. As the sintering temperature further increased to 2000 ℃ (HEBS-2000), stronger diffraction peaks of HEB and SiC phases were obtained, and the corresponding peak intensity ratio ($I_{\text{HEB-(101)HEBS-2000}}/I_{\text{HEB-(101)HEBS-1900}}$) of the (101) crystal plane for the HEB phase of HEBS-1900 and HEBS-2000 composites is calculated to 1.43 according to XRD data, and that of the (001) crystal plane for hexagonal SiC phase (PDF No. 51-0639) is 1.18, as shown in Table S1 in the Electronic Supplementary Material (ESM). The results suggest that the crystallinity of HEB and SiC phases become much better at higher temperatures (Fig. 7).

Figure 8 shows XRD Rietveld plots of the as-synthesized $(Ti_{0.2}Zr_{0.2}Hf_{0.2}Nb_{0.2}Ta_{0.2})B_2$–SiC powders and bulk ceramic composites. Comparatively, the phase composition of bulk ceramic composites is different from that of corresponding synthesized powders, which is attributed that the applied stress

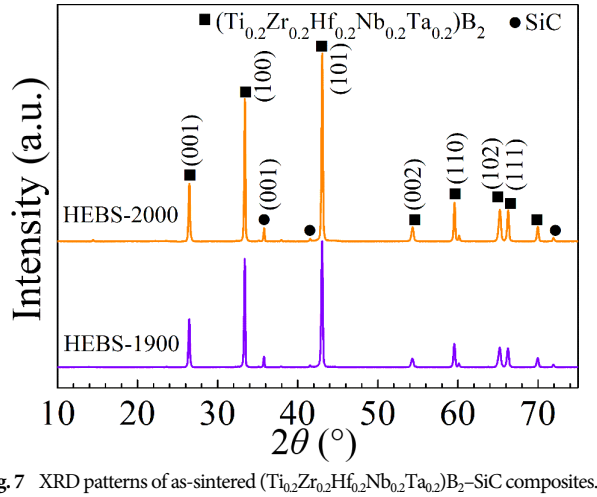

Fig. 7 XRD patterns of as-sintered $(Ti_{0.2}Zr_{0.2}Hf_{0.2}Nb_{0.2}Ta_{0.2})B_2$–SiC composites.

can facilitate the diffusion and solid solubility of Hf and Zr atoms into the HEB phase to form single-phase HEB during the reactive hot-pressing sintering [35]. The formed $(Ti_{0.2}Zr_{0.2}Hf_{0.2}Nb_{0.2}Ta_{0.2})B_2$ phase was refined using a hexagonal *P/6mmm* structure, which yields the lattice of $a = b = 3.0982$ Å, $c = 3.3706$ Å, and the SiC phase was also refined using a hexagonal structure. The theoretical density of $(Ti_{0.2}Zr_{0.2}Hf_{0.2}Nb_{0.2}Ta_{0.2})B_2$ was then calculated to be 8.24 g·cm^{-3}, which was consistent with the reported literature results (i.e., 8.24 g·cm^{-3}) [7].

Figure 9 shows back-scattered electron SEM (BSE-SEM) images of the HEBS-1900 and HEBS-2000 composites sintered at different temperatures. For the HEBS-1900 composites sintered at 1900 ℃ for 2 h, small grains (~1.5 μm) with a bright or dark contrast can be seen (Figs. 9(a)–9(c)), suggesting a variation in composition. Besides, micropores can be observed in the HEBS-1900 composites, and the relative density was comparatively low

to 96.5%. When the sintering temperature increased to 2000 ℃ (HEBS-2000), the grain sizes of both bright and dark phases are around ~2.0 μm (Figs. 9(d)–9(f)). This sample is free of micropores and microcracks, and the relative density reaches

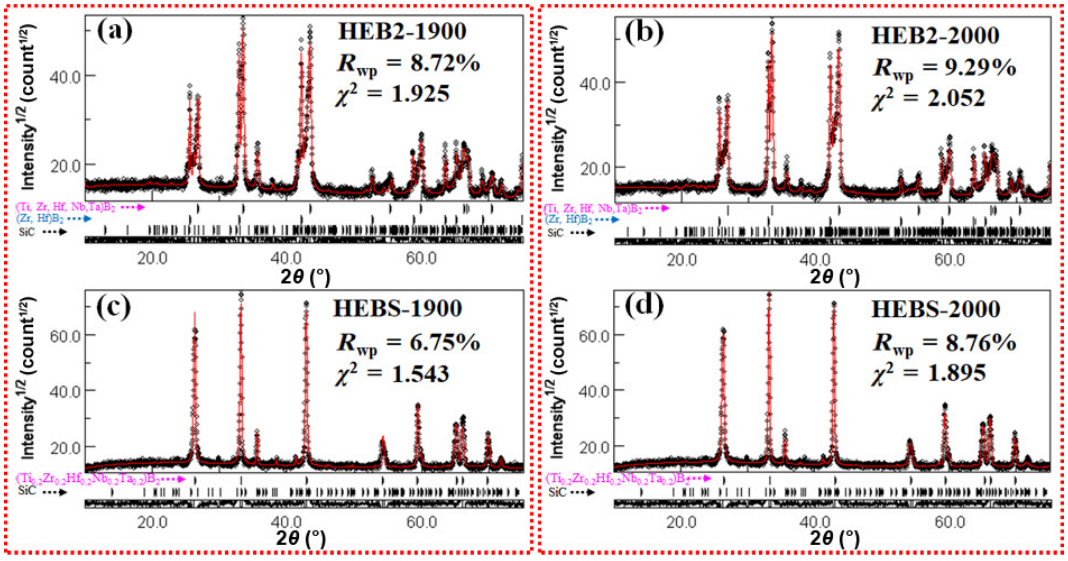

Fig. 8 XRD Rietveld plots of as-synthesized $(Ti_{0.2}Zr_{0.2}Hf_{0.2}Nb_{0.2}Ta_{0.2})B_2$–SiC powders and bulk ceramic composites: (a) HEB2-1900, (b) HEB2-2000, (c) HEBS-1900, and (d) HEBS-2000.

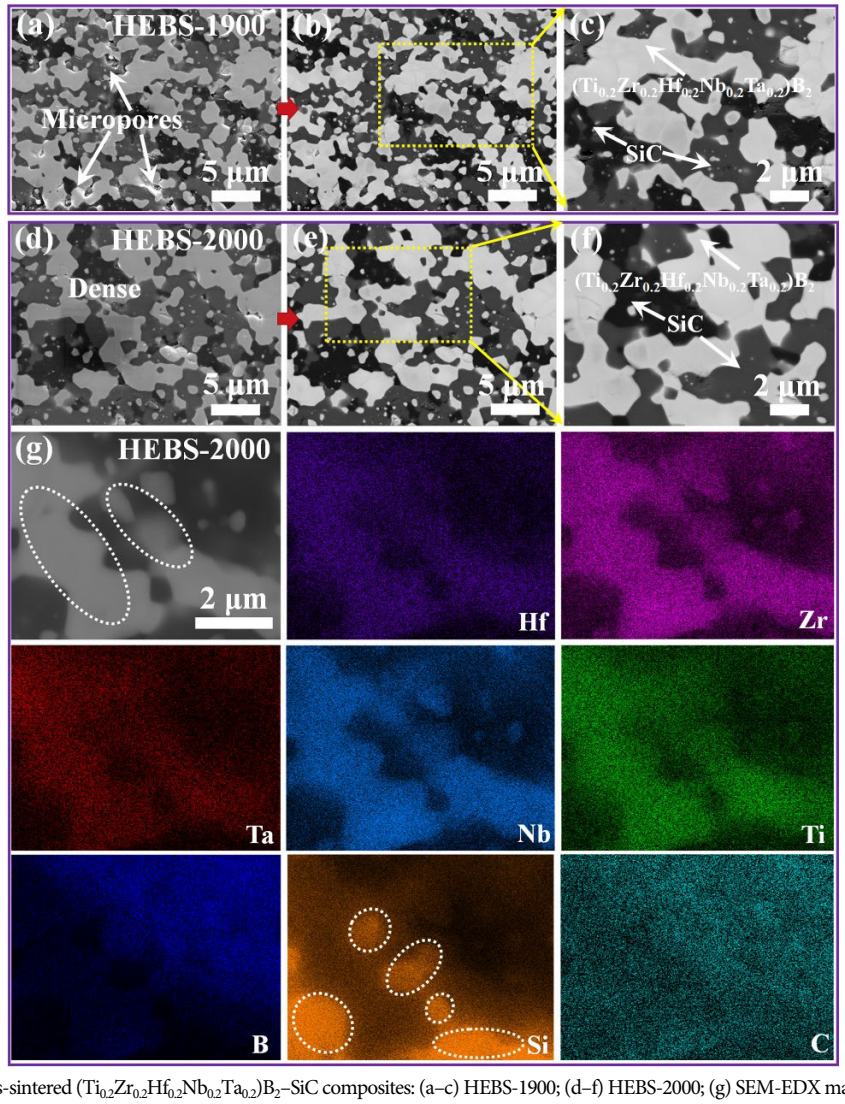

Fig. 9 BSE-SEM images of as-sintered $(Ti_{0.2}Zr_{0.2}Hf_{0.2}Nb_{0.2}Ta_{0.2})B_2$–SiC composites: (a–c) HEBS-1900; (d–f) HEBS-2000; (g) SEM-EDX mapping analyses of HEBS-2000 composites.

~99.3%. The darker phase is expected to be SiC, and the brighter one is $(Ti_{0.2}Zr_{0.2}Hf_{0.2}Nb_{0.2}Ta_{0.2})B_2$, which are also suggested by the SEM-EDX mapping analyses (Fig. 9(g)). The results show that $(Ti_{0.2}Zr_{0.2}Hf_{0.2}Nb_{0.2}Ta_{0.2})B_2$ and SiC grains are uniformly distributed in the HEBS-2000 composites, and the five metal elements Hf, Zr, Ta, Nb, and Ti are also homogeneous in the $(Ti_{0.2}Zr_{0.2}Hf_{0.2}Nb_{0.2}Ta_{0.2})B_2$ grain at the microscale scanned areas.

Figure 10(a) displays an STEM HAADF image of the HEBS-2000 composites. Together with the STEM-EDX mapping and area spectra analyses (Figs. 10(b)–10(l)), it can be observed that the bright grains in the *Z* contrast dominated STEM HAADF image mainly contain Hf, Zr, Ta, Nb, Ti, and B, which can be also confirmed by the STEM-EDX spectrum (Fig. 10(k), the squared area I in Fig. 10(a)). Selected area electron diffraction (SAED) analyses from these grains show a hexagonal AlB_2 structure (Fig. 11(c), the area I in Fig. 11(b)), and a set of lattice fringes with *d*-space of 0.33 nm corresponds to the (001) crystal plane for the zone axis (ZA) [011] of hexagonal $(Ti_{0.2}Zr_{0.2}Hf_{0.2}Nb_{0.2}Ta_{0.2})B_2$ phase (Fig. 11(d), the area I in Fig. 11(b)). The results are consistent with the crystal structure of $(Ti_{0.2}Zr_{0.2}Hf_{0.2}Nb_{0.2}Ta_{0.2})B_2$ identified with XRD analysis. In addition, the dark grains were identified by SAED to be hexagonal SiC (Fig. 11(e), the area II in Fig. 11(b)), and the HRTEM image shows a periodic lattice structure with a set of lattice fringes with *d*-space of 0.262 nm assigned to the (100) crystal plane of hexagonal SiC (Fig. 11(f)). It was also confirmed to be mainly composed of 69.1 at% Si, 26.50 at% C, and other minor elements (Fig. 10(l) and Table 2, the squared area II in Fig. 10(a)). It was evident that the five metal elements in the HEBS-2000 composites were also uniformly distributed at the nanoscale with a near equiatomic composition (Table 2, the squared area I in Fig. 10(a)). Simultaneously, the oxygen contents of HEB and SiC grains were 7.76 at% O (0.92 wt%) and 0.80 at% O (0.44 wt% O), respectively. Similarly, the oxygen content within the HEBS-2000 composites was evaluated to be 0.76 wt% using the element analyzer. Combining the XRD Rietveld refinement (Fig. 7) with imaging analyses, the phase contents of the HEBS-2000 composites were estimated to be ~71 wt% $(Ti_{0.2}Zr_{0.2}Hf_{0.2}Nb_{0.2}Ta_{0.2})B_2$, ~29 wt% SiC, and the corresponding volume fractions of the two phases were ~49 vol% $(Ti_{0.2}Zr_{0.2}Hf_{0.2}Nb_{0.2}Ta_{0.2})B_2$ and ~51 vol% SiC.

3.3 Mechanical properties of $(Ti_{0.2}Zr_{0.2}Hf_{0.2}Nb_{0.2}Ta_{0.2})B_2$–SiC composites

Figure 12 shows the Young's modulus and hardness of the as-sintered $(Ti_{0.2}Zr_{0.2}Hf_{0.2}Nb_{0.2}Ta_{0.2})B_2$–SiC composites. The modulus (Fig. 12(a)) and hardness (Fig. 12(b)) exhibited small increase trends with the increase of sintering temperatures through one-step BCTR reactive sintering, but the values were still comparable to those of the reported HEB ceramics [3,7,36]. The enhanced Young's modulus and hardness can be attributed to the highly sintering densification due to the fast matter transport for one-step BCTR reactive sintering [26,28]. Besides, the SiC secondary phase is uniformly incorporated in the HEB ceramics. The solid solution and composite structure may also contribute to the increase of modulus and hardness [3,31].

To investigate the crack propagation behavior, the indentation was also performed at different loads (5, 10, 15, 20, and 25 N) on the well-polished surface of the bulk ceramic samples. Figure S1 in the ESM shows the produced cracks at different loads in our experiments. The lengths of the radial cracks were then measured from the center of indentation prints using SEM. A total of 15 indentations were conducted on each sample. To calculate the fracture toughness, different model equations can be used

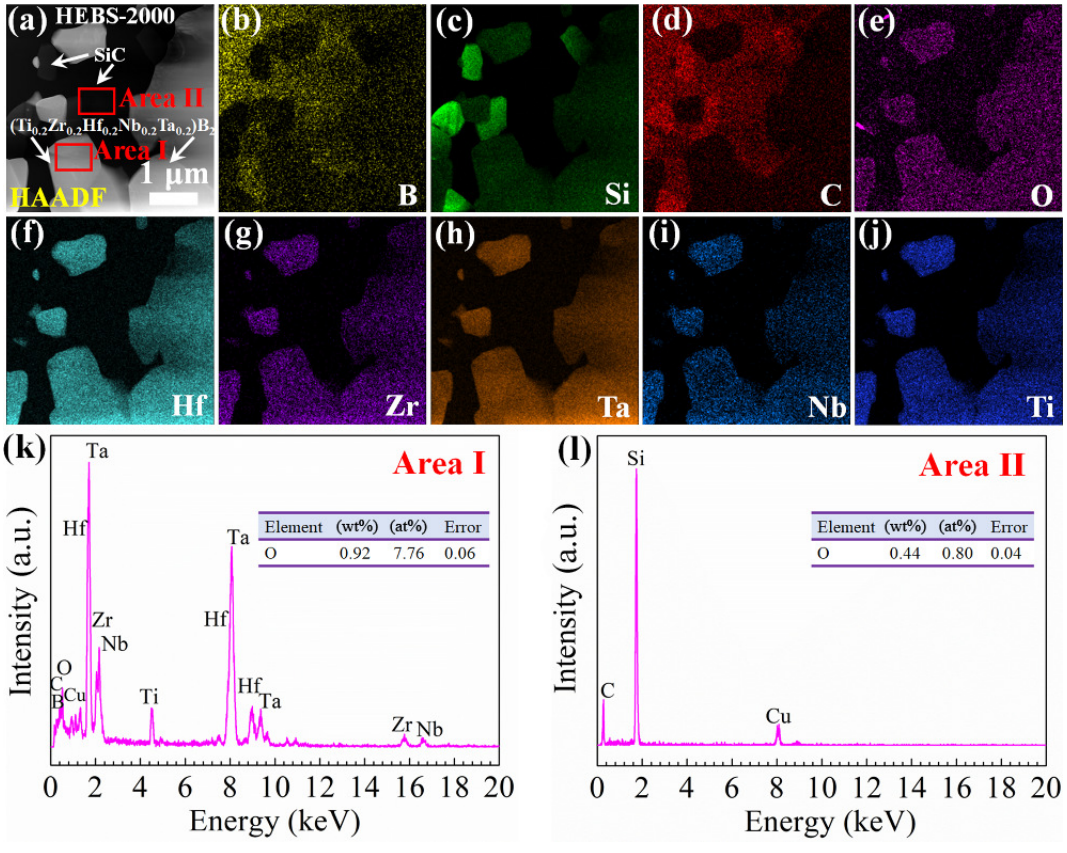

Fig. 10 (a) STEM HAADF image, (b–j) EDX mapping, and (k, l) EDX area analyses of HEBS-2000 composites.

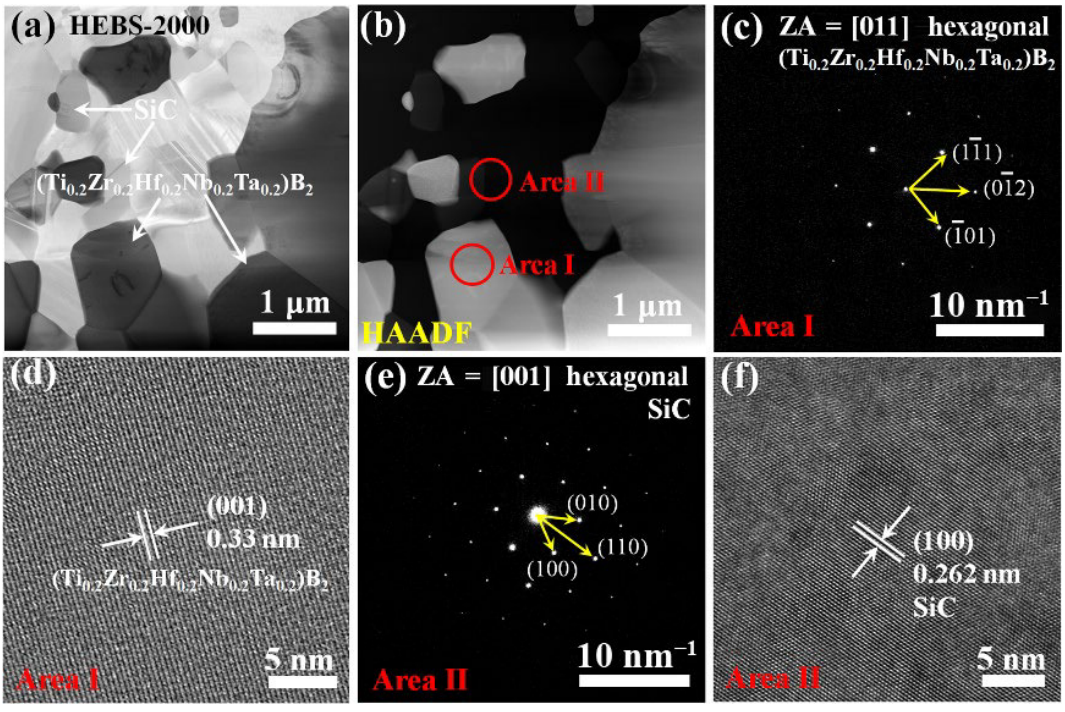

Fig. 11 (a) STEM BF; (b) HAADF image; SAED patterns: (c) area I in (b) and (e) area II in (b); HRTEM images: (d) area I in (b) and (f) area II in (b) of HEBS-2000 composites.

Table 2 Elemental compositions of different areas in HEBS-2000 composites that are shown in Fig. 10(b)

HEBS-2000 composite	Elemental composition (at%)								
	Hf	Zr	Ta	Nb	Ti	B	Si	C	O
Area I	13.3	13.1	13.5	12.0	12.2	32.96	—	—	2.94
Area II	0.66	0.29	1.81	0.06	0.06	0.72	69.10	26.50	0.80

depending on the crack system [37–41]. The type of cracks in both of $(Ti_{0.2}Zr_{0.2}Hf_{0.2}Nb_{0.2}Ta_{0.2})B_2$–SiC composites with different loads was determined to be radial-median cracks ($c/a \geq 3.5$) from SEM observation (Fig. S1 in the ESM). Moreover, the relationship between the crack length (l and c) and the loading force for $(Ti_{0.2}Zr_{0.2}Hf_{0.2}Nb_{0.2}Ta_{0.2})B_2$–SiC composites was plotted according to Eqs. (1) and (2) [41], as shown in Figs. 13(a) and 13(b), respectively.

For Palmqvist cracks:

$$l = AP \tag{1}$$

For radial-median cracks:

$$c = BP^{2/3} \tag{2}$$

where P is loading force (N); a, c, and l are crack length data (m), as shown in Fig. 11; A and B are the constants, which are related to Young's modulus, the hardness, and the fracture toughness of the ceramics and the indenter shape [41]. From the data of the $(Ti_{0.2}Zr_{0.2}Hf_{0.2}Nb_{0.2}Ta_{0.2})B_2$–SiC composites plotted in Figs. 13(a) and 13(b), it can be found that the radial-median crack is suitable to describe the cracks produced with the indentation. Therefore, K_{IC} values were calculated by the typical model equations applicable for both crack types in Table 3.

Figure 14 shows that K_{IC} evaluated by the Vickers indentation depends on the use of K_{IC} model equations. K_{IC} values of HEBS-1900 and HEBS-2000 composites varied in the ranges of 3.0–7.9 MPa·$m^{1/2}$ (Fig. 14(a)) and 4.5–9.4 MPa·$m^{1/2}$ (Fig. 14(b)), respectively. The value of 3.0–5.2 MPa·$m^{1/2}$ obtained using Eqs. (3) and (4) in Table 3 was considered to be more accurate for the HEBS-1900 composites as the calculated K_{IC} values nearly did not change with the indentation loading force, which is expected for microscopically dense samples as studied in the previous work [31]. For the HEBS-2000 composites, Eq. (5) in Table 3 gave

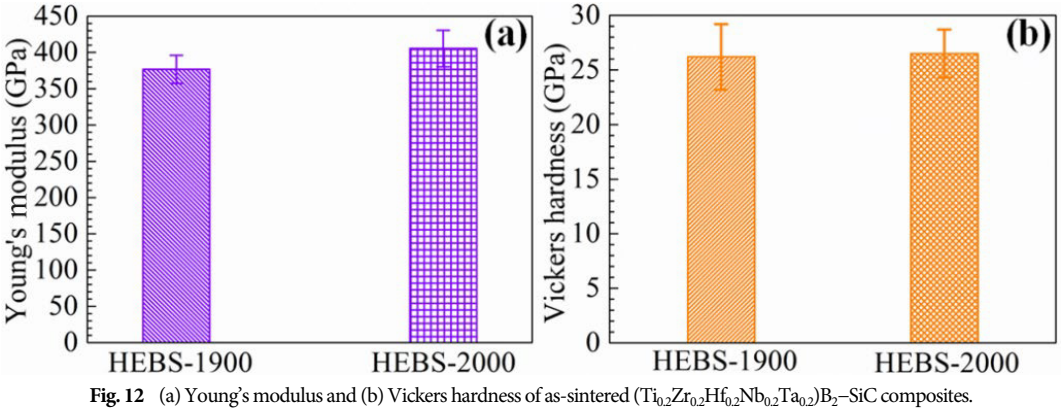

Fig. 12 (a) Young's modulus and (b) Vickers hardness of as-sintered $(Ti_{0.2}Zr_{0.2}Hf_{0.2}Nb_{0.2}Ta_{0.2})B_2$–SiC composites.

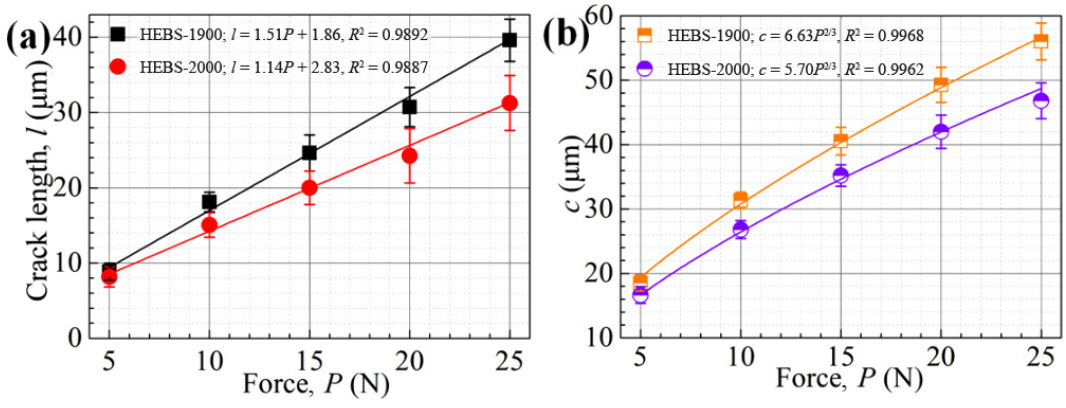

Fig. 13 Relationship between loading force and crack length produced using Vickers indentation in HEBS-1900 and HEBS-2000 composites for (a) Palmqvist cracks and (b) radial-median cracks.

Table 3 Typical model equations for calculating K_{IC} value from different crack types

Eq.	Author	Equation	Crack type
(3)	Shetty *et al.* (Ref. [37])	$K_{IC} = 0.0889(HP/41)^{0.5}$	Palmqvist ($l/a \le 2.5$ or $c/a \le 3.5$)
(4)	Tai (Ref. [38])	$K_{IC} = 0.0295H^{0.6}E^{0.4}a^{1.04}l^{-0.54}$	Palmqvist ($l/a \le 2.5$ or $c/a \le 3.5$)
(5)	Anstis *et al.* (Ref. [39])	$K_{IC} = 0.016(E/H)^{0.5}Pc^{-1.5}$	Radial-median ($c/a \ge 3.5$)
(6)	Evans and Charles (Ref. [40])	$K_{IC} = 0.057H^{0.6}E^{0.4}a^2c^{-1.5}$	Radial-median ($c/a \ge 3.5$)

Note: K_{IC} in MPa·m$^{1/2}$, H is the Meyer's hardness in GPa, $H = P/2a^2$, E is the Young's modulus in GPa, and P is the indentation load in N; a, c, and l are in m, as seen in Fig. S1 in the ESM.

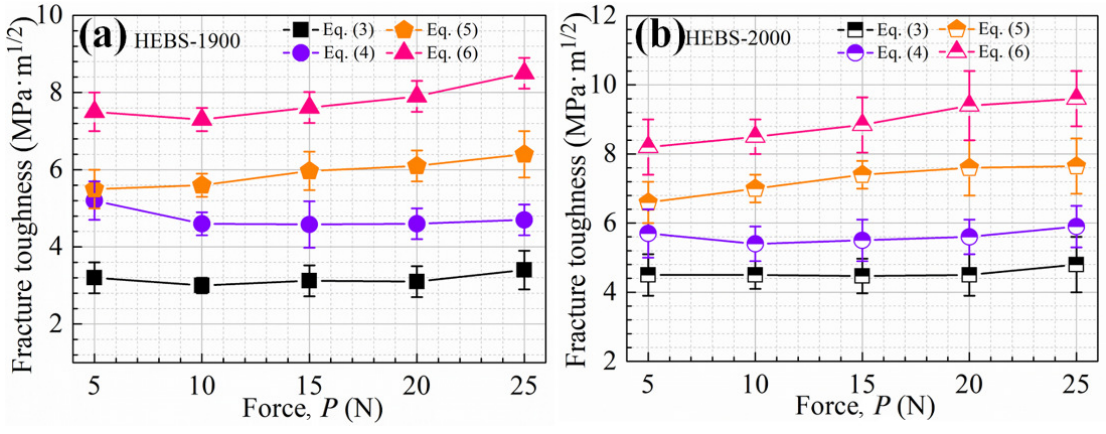

Fig. 14 Variation of mean fracture toughness of (a) HEBS-1900 and (b) HEBS-2000 composites as a function of loading forces using Vickers indentation.

comparatively stable K_{IC} values at higher loads. Therefore, a range of 6.6–7.7 MPa·m$^{1/2}$ was considered to be a reasonable estimation. The values obtained from the indentation method indicated that the fracture toughness of the $(Ti_{0.2}Zr_{0.2}Hf_{0.2}Nb_{0.2}Ta_{0.2})B_2$–SiC composites was greatly enhanced compared to the $(Ti_{0.2}Zr_{0.2}Hf_{0.2}Nb_{0.2}Ta_{0.2})B_2$ ceramics reported in the literature that employed also the indentation method for fracture toughness measurements [8,16,36], as shown in Table 4. The results showed that the indentation toughness of the fully dense HEBS-2000 composites in the current work was ~7.7 MPa·m$^{1/2}$, which was significantly higher than those of other $(Ti_{0.2}Zr_{0.2}Hf_{0.2}Nb_{0.2}Ta_{0.2})B_2$-based composites (Table 4), including $(Ti_{0.2}Zr_{0.2}Hf_{0.2}Nb_{0.2}Mo_{0.2})B_2$–20SiC composites (4.53±0.66 MPa·m$^{1/2}$) [4], $(Ti_{0.2}Zr_{0.2}Hf_{0.2}Nb_{0.2}Ta_{0.2})B_2$–20SiC composites (4.85±0.33 MPa·m$^{1/2}$) [8], SiC–15$(Ti_{0.2}Hf_{0.2}Nb_{0.2}Ta_{0.2}Mo_{0.2})B_2$ composites (4.88±0.88 MPa·m$^{1/2}$) [16], and $(Ti_{0.2}Zr_{0.2}Hf_{0.2}Nb_{0.2}Ta_{0.2})B_2$ (~5.3 MPa·m$^{1/2}$) [36].

The investigation of the crack propagation under indentation revealed several toughening mechanisms (Fig. 15). Typical crack deflection, bridging, and grain pullout behaviors were observed in the HEBS-2000 composites (Figs. 15(d)–15(f)), which could increase the tortuosity of the cracking path and enhance the resistance to the crack propagation [12,24]. Comparatively, for the HEBS-1900 composites, the straight cracking path could be seen (Fig. 15(a)), and only small-angle crack deflection can be observed (Figs. 15(b) and 15(c)). The main crack in the HEBS-1900 composites exhibited a larger gap than that of the HEBS-2000 composites (Figs. 15(c) and 15(f)).

4 Discussion

The unique SiB_6 additive has been employed to function as both boron and silicon sources, which was found to be able to react

Table 4 Comparison for Vickers hardness, Young's modulus, and fracture toughness of HEB-based ceramics from literature and this work

HEB-based ceramic	Vickers hardness (GPa)	Young's modulus (GPa)	Fracture toughness ($MPa \cdot m^{1/2}$)	Ref.
$(Ti_{0.2}Zr_{0.2}Hf_{0.2}Nb_{0.2}Mo_{0.2})B_2$–20SiC	25.8±1.2	—	4.53±0.66	[4]
$(Ti_{0.2}Zr_{0.2}Hf_{0.2}Nb_{0.2}Ta_{0.2})B_2$	22.44±0.56	~500	2.83±0.15	[6]
$(Ti_{0.2}Zr_{0.2}Hf_{0.2}Nb_{0.2}Ta_{0.2})B_2$	23.7±0.7	448	3.81±0.40	[8]
$(Ti_{0.2}Zr_{0.2}Hf_{0.2}Nb_{0.2}Ta_{0.2})B_2$–20SiC	24.8±1.2	419	4.85±0.33	[8]
$(Ti_{0.2}Zr_{0.2}Hf_{0.2}Nb_{0.2}Ta_{0.2})B_2$	21.7±1.1	—	4.06±0.35	[9]
$20(Ti_{0.2}Zr_{0.2}Hf_{0.2}Nb_{0.2}Ta_{0.2})B_2$–$80(Ti_{0.2}Zr_{0.2}Hf_{0.2}Nb_{0.2}Ta_{0.2})C$	24.2±0.3	—	3.19±0.24	[14]
$(Ti_{0.2}Hf_{0.2}Nb_{0.2}Ta_{0.2}Mo_{0.2})B_2$	16.6	—	3.10	[16]
SiC–$15(Ti_{0.2}Hf_{0.2}Nb_{0.2}Ta_{0.2}Mo_{0.2})B_2$	21.9±0.7	—	4.88±0.88	[16]
$(Ti_{0.2}Zr_{0.2}Hf_{0.2}Nb_{0.2}Ta_{0.2})B_2$	26.2	—	5.3	[36]
$(ZrHfNbTaMoW)B_2$	33.1±1.1	520±12	3.9±1.2	[42]
$(Ti_{0.2}Zr_{0.2}Hf_{0.2}Nb_{0.2}Ta_{0.2})B_2$	19.4±1.3	524.6±6.9	—	[43]
HEBS-1900	26.2±3.0	376.8±19.3	~5.2	This work
HEBS-2000 ($49(Ti_{0.2}Zr_{0.2}Hf_{0.2}Nb_{0.2}Ta_{0.2})B_2$–51SiC)	26.5±2.2	405.5±25.2	~7.6	This work

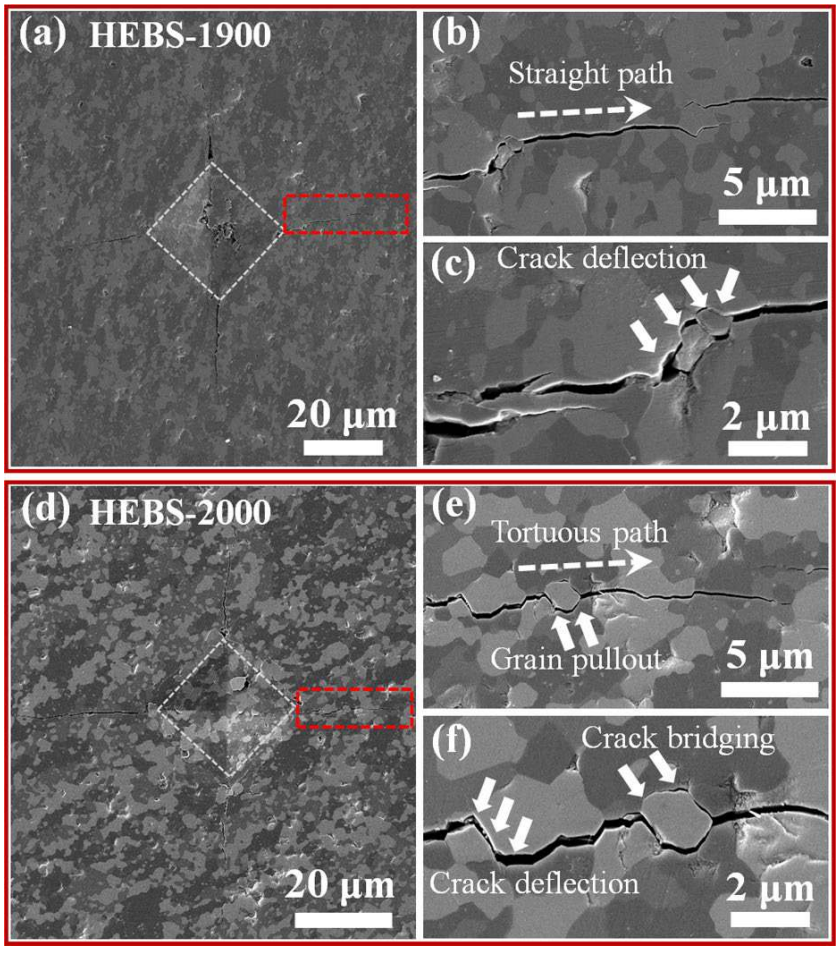

Fig. 15 (a–c) Crack propagation behaviors of HEBS-1900 and (d–f) HEBS-2000 composites during Vickers indentation tests.

with transition metal oxides and nano-carbon to produce (Ti,Zr,Hf,Nb,Ta)B_2–SiC composite powders through one-step BCTR route. As the synthesis temperature increased from 1900 to 2000 ℃, the amount of impurity phase was decreased presumably due to an enhanced elemental diffusion and mass transport required for solid solution formation [26–28]. Borides were oxidized to form liquid B_2O_3, which promoted the generation of a liquid bridge between particles known as necking [33]. However, the formation of necking and solid solution has also been reported to facilitate the mass transport [10,25,43], resulting in the particle sintering and agglomeration to form nanoparticle clusters, as observed in STEM images (Figs. 3(a), 3(d), and 4(a)). The formed nanoparticle clusters in the (Ti,Zr,Hf,Nb,Ta)B_2–SiC powders were composed of ~200 nm particles, which finally led to the increase of their tested particle sizes into microscale sizes from 8.0±0.2 μm (HEB2-1900) to 9.0±0.2 μm (HEB4-2000).

To understand the formation mechanism associated with $(Ti_{0.2}Zr_{0.2}Hf_{0.2}Nb_{0.2}Ta_{0.2})B_2$ and SiC phases, six possible chemical

reactions during the BCTR described as Eqs. (7)–(12) are considered and the change in Gibbs free energy (ΔG_T, kJ·mol^{-1}) for the reactions are calculated according to Eq. (13):

$$TiO_2(s) + \frac{1}{3}SiB_6(s) + \frac{7}{3}C(s) \rightarrow TiB_2(s) + \frac{1}{3}SiC(l) + 2CO(g) \uparrow \quad (7)$$

$$ZrO_2(s) + \frac{1}{3}SiB_6(s) + \frac{7}{3}C(s) \rightarrow ZrB_2(s) + \frac{1}{3}SiC(l) + 2CO(g) \uparrow \quad (8)$$

$$HfO_2(s) + \frac{1}{3}SiB_6(s) + \frac{7}{3}C(s) \rightarrow HfB_2(s) + \frac{1}{3}SiC(s) + 2CO(g) \uparrow \quad (9)$$

$$\frac{1}{2}Nb_2O_5(s) + \frac{1}{3}SiB_6(s) + \frac{17}{6}C(s) \rightarrow NbB_2(s) + \frac{1}{3}SiC(l) + \frac{5}{2}CO(g) \uparrow \quad (10)$$

$$\frac{1}{2}Ta_2O_5(s) + \frac{1}{3}SiB_6(s) + \frac{17}{6}C(s) \rightarrow TaB_2(s) + \frac{1}{3}SiC(l) + \frac{5}{2}CO(g) \uparrow \quad (11)$$

$$\frac{1}{5}HfB_2(s) + \frac{1}{5}ZrB_2(s) + \frac{1}{5}TaB_2(s) + \frac{1}{5}NbB_2(s) + \frac{1}{5}TiB_2(s) \rightarrow (Hf_{0.2}Zr_{0.2}Ta_{0.2}Nb_{0.2}Ti_{0.2})B_2(s) \quad (12)$$

$$\Delta G_T = \sum_i \nu_i \Delta_f G_T^\theta(i) + RT\ln\left[\frac{\prod_f \left(\frac{p_f}{p^\theta}\right)^{\nu_f}}{\prod_r \left(\frac{p_r}{p^\theta}\right)^{\nu_r}}\right] \quad (13)$$

where $\Delta_f G_T^\theta(i)$ is the Gibbs formation free energy for each compound (kJ·mol^{-1}); ν_i is the coefficient of reactants or products; ΔG_T is the change in Gibbs free energy of the reaction at different temperatures under vacuum atmosphere (1.0×10^{-2} Pa) (kJ·mol^{-1}); R is the ideal gas constant (J·mol^{-1}·K^{-1}); T is the temperature (K); p_f is the gas product pressure (Pa); p_r is the gas reactant pressure (Pa); P^θ is the standard pressure (1.0×10^5 Pa), and ν_r is the coefficient of reactants; ν_f is the coefficient of product. In this case, the partial pressure of the gas product CO is considered to be equal to the furnace vacuum atmosphere (1.0×10^{-2} Pa).

The changes in the Gibbs free energy for reactions as a function of the temperature under the furnace vacuum atmosphere are plotted in Fig. 16. The onset temperatures of the reactions (Eqs. (7)–(10)) were predicted with the furnace vacuum atmosphere considered. It can be found that the onset temperatures of above 700 ℃ for reactions of Eqs. (8) and (9) in the synthesis of ZrB_2 and HfB_2 were higher than those of the other three diborides under the vacuum atmosphere of 1.0×10^{-2} Pa, which revealed that the formation of ZrB_2 and HfB_2 was more difficult than TiB_2, TaB_2, and NbB_2. It is clear that the changes in the Gibbs free energy of all the reactions (Eqs. (7)–(11)) are negative ($\Delta G_T < 0$) beyond 700 ℃, and thus they can all proceed spontaneously (Fig. 16). Reacted powders were subsequently heated to higher temperatures to promote solid solution

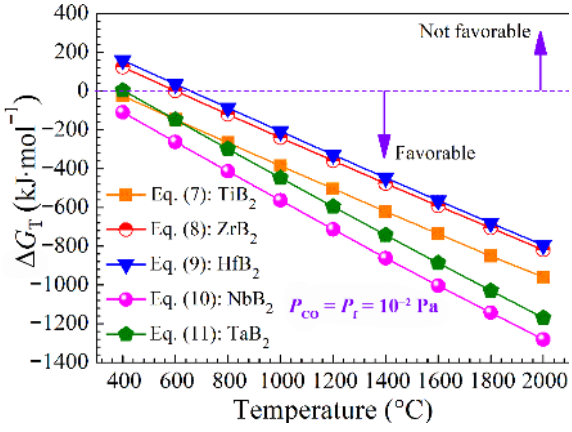

Fig. 16 Changes in Gibbs free energy for reactions as a function of temperature under furnace vacuum atmosphere ($P_{CO} = 1.0\times10^{-2}$ Pa).

formation (Eq. (12)) [21,25]. The results revealed that the synthesis of two-phase $(Ti_{0.2}Zr_{0.2}Hf_{0.2}Nb_{0.2}Ta_{0.2})B_2$–SiC composites through one-step BCTR with a SiB_6 additive was possible from the thermodynamic perspective, and it is feasible for SiB_6 to react with transitional metal oxides and nano-carbon to simultaneously form $(Ti_{0.2}Zr_{0.2}Hf_{0.2}Nb_{0.2}Ta_{0.2})B_2$ and SiC phases, leading to homogeneously distributed HEB–SiC composites. On the other hand, the three powder samples of HEB2-1900, HEB2-2000, and HEB4-2000 contained (Ti,Zr,Hf,Nb,Ta)B_2, SiC, and minor (Zr,Hf)B_2 impurity (Fig. 1). The presence of the (Zr,Hf)B_2 impurity can be attributed as follows: (i) the reactions for the synthesis of TiB_2, NbB_2, and TaB_2 firstly occurred to consume more SiB_6 than the normal quantities for the stoichiometric ratio due to the borides oxidation and further volatilization of B_2O_3, resulting in the insufficient boron source of SiB_6 for the reaction between ZrO_2 and HfO_2. This would kinetically lead to the formation of ZrB_2 and HfB_2 later. The part of the formed ZrB_2 and HfB_2 could not dissolved into the HEB phase, and separately produced solid solution of (Zr,Hf)B_2 [17,25]; (ii) SiB_6 as boron and silicon sources exhibited the larger particle size (3–8 μm) than that of B_4C (~2 μm) used as boron sources in the synthesis of HEB powders [17,44], which retarded the solid-state diffusion for the formation of single-phase solid solution, leading to the separation of (Zr,Hf)B_2 from HEB phase [44]; (iii) HfB_2 and ZrB_2 were more difficult to be dissolved into the HEB phase for producing the single-phase solid solution, which was due to their larger lattice parameters for easily causing large lattice distortion [26,45].

The unique SiB_6 additive was also effective as the boron and silicon sources to fabricate the bulk $(Ti_{0.2}Zr_{0.2}Hf_{0.2}Nb_{0.2}Ta_{0.2})B_2$–SiC composites through one-step BCTR reactive sintering. The applied stress and sintering temperature played an important role in solid solution formation, grain growth, and densification of bulk $(Ti_{0.2}Zr_{0.2}Hf_{0.2}Nb_{0.2}Ta_{0.2})B_2$–SiC composites. Compared with the synthesis of (Ti,Zr,Hf,Nb,Ta)B_2–SiC powders through reactive pressureless sintering, the chemical potential of the atoms under the contact surfaces increased in the presence of B_2O_3 liquid with the applied stress during reactive hot pressing sintering, which enhanced the mass transport from the contact regions to the pores, thereby leading to an increase in the densification rate of the $(Ti_{0.2}Zr_{0.2}Hf_{0.2}Nb_{0.2}Ta_{0.2})B_2$–SiC composites [46]. Besides, both lattice diffusion from grain boundary and grain boundary diffusion were promoted under the sintering stress at intermediate and final sintering stage [35], which could facilitate the diffusion and solid solubility of Hf and Zr atoms into the HEB phase to form a single-phase HEB. Simultaneously, surface diffusion and grain boundary diffusion with the viscous and plastic flow in a

liquid phase system can promote the formation and growth of the neck between spherical particles [35,47]. This process also promoted the sintering densification of the $(Ti_{0.2}Zr_{0.2}Hf_{0.2}Nb_{0.2}Ta_{0.2})B_2$–SiC composites. Additionally, as the sintering temperature increased to 2000 ℃, the high sintering temperature overcame the single-phase HEB phase formation barriers, which were the presence of strong B–B rings and TM–B (transitional metals, TM = Ti, Zr, Hf, Nb, and Ta) bonding, also together with the larger lattice parameters of HfB_2 and ZrB_2 [26,48]. The high sintering temperature also promoted the dissolution process of the binary diboride solid solution into the HEB crystal structure to form a complete single-phase HEB [49], accelerating the particle rearrangement, mass transport, and densification of the $(Ti_{0.2}Zr_{0.2}Hf_{0.2}Nb_{0.2}Ta_{0.2})B_2$–SiC composites at 2000 ℃. Simultaneously, the crystallinity of the HEBS-2000 composites exhibited a large improvement compared to that of the HEBS-1900 composites due to the higher sintering driving force (Fig. 8). A synergetic effect of the sluggish diffusion and the incorporation of SiC phase retarded the grain growth of HEBS-1900 and HEBS-2000 composites [17]. The SiC phase asserted a larger pinning pressure at the grain boundary, resulting in slower grain boundary motion and smaller grain size (~2.0 μm, Fig. 9). The small grain size is beneficial to shorten the diffusion path for mass transport, thereby increasing the rate of densification for achieving near-fully densification (~99.3%) in the HEBS-2000 composites [49,50].

In monolithic brittle HEB ceramics, the densification and grain refinement are beneficial for the improvement of mechanical properties fundamentally due to the decrease in the critical flaw size. The improvement in the mechanical properties is firstly related to the enhanced densification, which can reduce the flaw size of the composite ceramics to improve the mechanical properties [51]. The enhanced densification can be related to several mechanisms as discussed below. (1) During the one-step BCTR reactive sintering, SiB_6 reacted *in-situ* with transitional metal oxides and nano-carbon to form $(Ti_{0.2}Zr_{0.2}Hf_{0.2}Nb_{0.2}Ta_{0.2})B_2$–SiC composites, which can facilitate the mass transport across different phases compared to sintering of an HEB and SiC powder mixture, resulting in the enhanced densification [15,26,31]. (2) The oxide impurities in the particle surface and grain boundaries were removed with the addition of SiB_6 and nano-carbon, which is beneficial for enhancing the surface/grain boundary diffusion, also promoting densification [24,27,31]. Secondly, the formation of the dense high-entropy solid solution can provide a strengthening effect to enhance the hardness of HEB-based composites. Young's modulus followed the same trend as hardness in all samples. Meanwhile, a synergetic effect of grain refinement and SiC secondary phase also contributed to the increase of fracture toughness. These fine grains can serve as energy-dissipation zones resulting in higher indentation toughness in the HEB-based composites [52]. Lastly, the improvement of fracture toughness is believed to be related to the different crack propagation modes observed in the HEBS-2000 composites compared to the HEBS-1900 composites. The predominant crack propagation mode of the HEBS-1900 sample was transgranular cracking, resulting in the straight crack propagation path (Figs. 15(b) and 15(c)). An initial plane cleavage crack intersected and propagated across a grain boundary between two otherwise perfect grains in the transgranular cracking [53]. Although it was reported that the resistance was determined by the type and degree of the cleavage-plane rotation, the cracking was to remain on its preferred cleavage plane and linked by cleavage steps to form the straight crack path without the obvious cleavage-plane rotation [53]. The single transgranular cracking with a straight crack path cannot provide an effective toughening effect in HEBS-1900 composites. Similarly, the crack deflection by the intergranular crack in a homogeneous structure is not very effective way to lead to a crack bridge [54,55]. Some of the micropores were observed to remain in $(Ti_{0.2}Zr_{0.2}Hf_{0.2}Nb_{0.2}Ta_{0.2})B_2$/SiC and $(Ti_{0.2}Zr_{0.2}Hf_{0.2}Nb_{0.2}Ta_{0.2})B_2$/$(Ti_{0.2}Zr_{0.2}Hf_{0.2}Nb_{0.2}Ta_{0.2})B_2$ grain boundaries (Figs. 9(a) and 9(b)), weakening the grain boundaries, which can serve as sites for preferable crack initiation and propagation [56,57].

However, in the HEBS-2000 composites, the dominating cracking mode shifted from intergranular to a mixture mode of intergranular and transgranular cracking accompanied by the indication of grain bridging and pullout (Figs. 15(e) and 15(f)). This reveals that higher density leads to stronger grain boundaries, leading to some degree of transgranular cracking along the cleavage steps. In the mixed cracking mode, the enhanced grain boundary strength can help to improve the global fracture toughness as it has been shown to increase with grain boundary toughness (r_{gb}) increasing when r_{gb} is below approximately 1/2 of the grain fracture toughness (r_g) [54]. Meanwhile, although the intergranular fracture has been considered to be beneficial for toughening due to crack deflection, it has been also shown that the crack deflection alone is not an effective toughening mechanism unless crack bridging is activated under a condition that a sufficiently high proportion of cracks are deflected at large angles [55]. A similar positive effect of the transgranular cracking on the toughening was also reported in our previous studies, where a transition from intergranular to transgranular cracking was shown to increase the fracture toughness in HfC–HfB_2 and HfC–SiCN composites [31,50]. Therefore, when the grain boundary strength is optimized to introduce a suitable amount of transgranular fracture, the surface energy of the transgranular cracks could overcompensate for the reduced crack propagation length and result in higher fracture toughness. The crack deflection with larger angles could also happen along the cleavage steps and effectively pin the crack tip during transgranular cracking [53], which can contribute to the crack bridging process (Fig. 15(f)).

5 Conclusions

In summary, both $(Ti_{0.2}Zr_{0.2}Hf_{0.2}Nb_{0.2}Ta_{0.2})B_2$–SiC powders and dense bulk materials with a composite microstructure were successfully fabricated by one-step BCTR reactive sintering with a unique SiB_6 additive, which functions as both boron and silicon sources. Importantly, the near-fully dense composite microstructure could be achieved to give rise to a significant increase in fracture toughness. The following conclusions can be drawn:

(1) The particle size of the HEB2-1900 powder sample was ~200 nm, and can be increased to only ~500 nm fabricated at 2000 ℃ for 2 h (HEB2-2000) by BCTR reaction, which indicates that the BCTR process can promote the particle size reduction and intermixing through the reduction in diffusion distance between the reactants. However, with the holding time increasing to 4 h for 2000 ℃, the particle sintering occurred in the HEB4-2000 sample, resulting in the particle coarsening.

(2) A synergetic effect of sluggish diffusion and the incorporation of the SiC phase retarded the grain growth of the HEBS-1900 and HEBS-2000 composites. The SiC phase asserted a larger pinning pressure at the grain boundary, resulting in slower grain boundary motion and smaller grain size (~2.0 μm). The small grain size was beneficial to the shortened diffusion path for

mass transport, thereby increasing the composites densification to ~99.3%.

(3) The HEBS-2000 composites exhibited the significantly higher fracture toughness of ~7.7 MPa·m$^{1/2}$ than that of HEBS-1900 composites (~5.2 MPa·m$^{1/2}$), which corresponded to a large improvement of 48%. Apart from the improved densification, a synergetic effect of grain refinement, incorporation of the SiC secondary phase, and the grain boundary strength modification also contributed to the increase of fracture toughness. This work will open up a new research field that focuses on the fabrication of HEB-based composite powders and bulk materials, and searching for a rational microstructure design for their optimized mechanical properties.

Acknowledgements

This work has been supported by the National Natural Science Foundation of China (No. 52072238) and Key Research and Development Program of Zhejiang Province (No. 2022C01139).

Declaration of competing interest

The authors have no competing interests to declare that are relevant to the content of this article.

Electronic Supplementary Material

Supplementary material is available in the online version of this article at https://doi.org/10.26599/JAC.2024.9220838.

References

[1] Xiang HM, Xing Y, Dai FZ, *et al.* High-entropy ceramics: Present status, challenges, and a look forward. *J Adv Ceram* 2021, **10**: 385–441.

[2] Nisar A, Zhang C, Boesl B, *et al.* A perspective on challenges and opportunities in developing high entropy-ultra high temperature ceramics. *Ceram Int* 2020, **46**: 25845–25853.

[3] Gild J, Zhang YY, Harrington T, *et al.* High-entropy metal diborides: A new class of high-entropy materials and a new type of ultrahigh temperature ceramics. *Sci Rep* 2016, **6**: 37946.

[4] Zhang Y, Sun SK, Guo WM, *et al.* Optimal preparation of high-entropy boride–silicon carbide ceramics. *J Adv Ceram* 2021, **10**: 173–180.

[5] Liu D, Liu HH, Ning SS, *et al.* Chrysanthemum-like high-entropy diboride nanoflowers: A new class of high-entropy nanomaterials. *J Adv Ceram* 2020, **9**: 339–348.

[6] Gu JF, Zou J, Sun SK, *et al.* Dense and pure high-entropy metal diboride ceramics sintered from self-synthesized powders via boro/carbothermal reduction approach. *Sci China Mater* 2019, **62**: 1898–1909.

[7] Ni DW, Cheng Y, Zhang JP, *et al.* Advances in ultra-high temperature ceramics, composites, and coatings. *J Adv Ceram* 2022, **11**: 1–56.

[8] Liu JX, Shen XQ, Wu Y, *et al.* Mechanical properties of hot-pressed high-entropy diboride-based ceramics. *J Adv Ceram* 2020, **9**: 503–510.

[9] Zhang Y, Jiang ZB, Sun SK, *et al.* Microstructure and mechanical properties of high-entropy borides derived from boro/carbothermal reduction. *J Eur Ceram Soc* 2019, **39**: 3920–3924.

[10] Yang ZG, Gong YB, Zhang SQ, *et al.* Microstructure and properties of high-entropy diboride composites prepared by pressureless sintering. *J Alloys Compd* 2023, **952**: 169975.

[11] Meng JW, Fang HY, Wang HY, *et al.* Effects of refractory metal additives on diboride-based ultra-high temperature ceramics: A review. *Int J Appl Ceram Technol* 2023, **20**: 1350–1370.

[12] Bannykh D, Utkin A, Baklanova N. The peculiarities in oxidation behavior of the ZrB_2–SiC ceramics with chromium additive. *Int J Refract Met H* 2019, **84**: 105023.

[13] Sun CN, Baldridge T, Gupta MC. Fabrication of ZrB_2–Zr cermet using laser sintering technique. *Mater Lett* 2009, **63**: 2529–2531.

[14] Luo SC, Guo WM, Plucknett K, *et al.* Fine-grained dual-phase high-entropy ceramics derived from boro/carbothermal reduction. *J Eur Ceram Soc* 2021, **41**: 3189–3195.

[15] Huo SJ, Chen L, Liu XR, *et al.* Reactive sintering of dual-phase high-entropy ceramics with superior mechanical properties. *J Mater Sci Technol* 2022, **129**: 223–227.

[16] Yuan JH, Guo WM, Liu Y, *et al.* Hardness and toughness improvement of SiC-based ceramics with the addition of $(Hf_{0.2}Mo_{0.2}Ta_{0.2}Nb_{0.2}Ti_{0.2})B_2$. *J Am Ceram Soc* 2022, **105**: 1629–1634.

[17] Shen XQ, Liu JX, Li F, *et al.* Preparation and characterization of diboride-based high entropy $(Ti_{0.2}Zr_{0.2}Hf_{0.2}Nb_{0.2}Ta_{0.2})B_2$–SiC particulate composites. *Ceram Int* 2019, **45**: 24508–24514.

[18] Lu K, Liu JX, Wei XF, *et al.* Microstructures and mechanical properties of high-entropy $(Ti_{0.2}Zr_{0.2}Hf_{0.2}Nb_{0.2}Ta_{0.2})C$ ceramics with the addition of SiC secondary phase. *J Eur Ceram Soc* 2020, **40**: 1839–1847.

[19] Zhang P, Cheng CY, Liu B, *et al.* Multicomponent $(Hf_{0.25}Zr_{0.25}Ti_{0.25}Cr_{0.25})B_2$ ceramic modified SiC–Si composite coatings: *In-situ* synthesis and high-temperature oxidation behavior. *Ceram Int* 2022, **48**: 12608–12624.

[20] Tallarita G, Licheri R, Garroni S, *et al.* Novel processing route for the fabrication of bulk high-entropy metal diborides. *Scripta Mater* 2019, **158**: 100–104.

[21] Liu D, Wen TQ, Ye BL, *et al.* Synthesis of superfine high-entropy metal diboride powders. *Scripta Mater* 2019, **167**: 110–114.

[22] Ye BL, Fan C, Han YJ, *et al.* Synthesis of high-entropy diboride nanopowders via molten salt-mediated magnesiothermic reduction. *J Am Ceram Soc* 2020, **103**: 4738–4741.

[23] Yang Y, Bi JQ, Gao XC, *et al.* Facile synthesis of nanocrystalline high-entropy diboride powders by a simple sol–gel method and their performance in supercapacitor. *Ceram Int* 2023, **49**: 19523–19527.

[24] Liu D, Liu HH, Ning SS, *et al.* Synthesis of high-purity high-entropy metal diboride powders by boro/carbothermal reduction. *J Am Ceram Soc* 2019, **102**: 7071–7076.

[25] Feng L, Fahrenholtz WG, Hilmas GE. Two-step synthesis process for high-entropy diboride powders. *J Am Ceram Soc* 2020, **103**: 724–730.

[26] Feng L, Fahrenholtz WG, Hilmas GE, *et al.* Boro/carbothermal reduction co-synthesis of dual-phase high-entropy boride-carbide ceramics. *J Eur Ceram Soc* 2023, **43**: 2708–2712.

[27] Zhu SM, Fahrenholtz WG, Hilmas GE, *et al.* Pressureless sintering of zirconium diboride using boron carbide and carbon additions. *J Am Ceram Soc* 2007, **90**: 3660–3663.

[28] Smith SM II, Feng L, Fahrenholtz WG, *et al.* High-entropy boride–carbide ceramics by sequential boro/carbothermal synthesis. *J Am Ceram Soc* 2022, **105**: 5543–5547.

[29] Gong YB, Yang ZG, Wei XG, *et al.* Synthesis and electromagnetic wave absorbing properties of high-entropy metal diboride–silicon carbide composite powders. *J Mater Sci* 2022, **57**: 9218–9230.

[30] Hao W, Ni N, Liu TY, *et al.* Ablation resistance of HfC(Si,O)–HfB_2 (Si,O) composites fabricated by one-step reactive spark plasma sintering. *J Eur Ceram Soc* 2021, **41**: 2226–2238.

[31] Hao W, Ni N, Guo Y, *et al.* Strong and tough HfC–HfB_2 solid–solution composites obtained by reactive sintering with a SiB_6 additive. *Ceram Int* 2020, **46**: 16257–16265.

[32] Lutterotti L. Maud version 2.9993. Available at https://luttero.github.io/maud/

[33] Mazlan MR, Jamadon NH, Rajabi A, *et al.* Necking mechanism under various sintering process parameters—A review. *J Mater Res Technol* 2023, **23**: 2189–2201.

[34] Zhang Y, Wu LM, El-Mounayri H, *et al.* Molecular dynamics study of the strength of laser sintered iron nanoparticles. *Procedia Manuf* 2015, **1**: 296–307.

[35] Rahaman MN. *Sintering of Ceramics*. New York: Taylor and Francis, 2007.

[36] Ma MD, Ye BL, Han YJ, *et al.* High-pressure sintering of ultrafine-grained high-entropy diboride ceramics. *J Am Ceram Soc* 2020, **103**: 6655–6658.

[37] Shetty DK, Wright IG, Mincer PN, *et al.* Indentation fracture of WC-Co cermets. *J Mater Sci* 1985, **20**: 1873–1882.
[38] Tai Q. The research on K_{IC} values for several kinds of high temperature structural ceramics by indentation method. *Bull Chin Ceram Soc* 1990, **3**: 44–50.
[39] Anstis GR, Chantikul P, Lawn BR, *et al.* A critical evaluation of indentation techniques for measuring fracture toughness: I, direct crack measurements. *J Am Ceram Soc* 1981, **64**: 533–538.
[40] Evans AG, Charles EA. Fracture toughness determinations by indentation. *J Am Ceram Soc* 1976, **59**: 371–372.
[41] Song K, Xu YH, Zhao NN, *et al.* Evaluation of fracture toughness of tantalum carbide ceramic layer: A vickers indentation method. *J Mater Eng Perform* 2016, **25**: 3057–3064.
[42] Murchie AC, Watts JL, Fahrenholtz WG, *et al.* Room-temperature mechanical properties of a high-entropy diboride. *Int J Appl Ceram Technol* 2022, **19**: 2293–2299.
[43] Qin MD, Gild J, Hu CZ, *et al.* Dual-phase high-entropy ultra-high temperature ceramics. *J Eur Ceram Soc* 2020, **40**: 5037–5050.
[44] Yang Y, Bi JQ, Sun KN, *et al.* Novel $(Hf_{0.2}Zr_{0.2}Ta_{0.2}V_{0.2}Nb_{0.2})B_2$ high entropy diborides with superb hardness sintered by SPS under a mild condition. *Ceram Int* 2022, **48**: 30859–30867.
[45] Xu L, Huang KH, Guo WM, *et al.* B_4C–(Hf,Zr,Ta,Nb,Ti)B_2 composites prepared by reactive and non-reactive spark plasma sintering. *Ceram Int* 2023, **49**: 19556–19560.
[46] Rahaman MN. *Ceramic Processing and Sintering*. New York: Taylor and Francis, 2003.
[47] Milman YV, Slipenyuk AN. The role of plastic deformation in the process of powder sintering. *Solid State Phenom* 2006, **114**: 199–210.
[48] Zhang Z, Zhu SZ, Liu YB, *et al.* Enthalpy driving force and chemical bond weakening: The solid-solution formation mechanism and densification behavior of high-entropy diborides $(Hf_{1-x/4}Zr_{1-x/4}Nb_{1-x/4}Ta_{1-x/4}Sc_x)B_2$. *J Eur Ceram Soc* 2022, **42**: 3685–3698.
[49] Xu L, Guo WM, Zou J, *et al.* Low-temperature densification of high entropy diboride based composites with fine grains and excellent mechanical properties. *Compos Part B Eng* 2022, **247**: 110331.
[50] Hao W, Ni N, Guo Y, *et al.* Densification, strengthening and toughening in hafnium carbide with the addition of silicon carbonitride. *J Am Ceram Soc* 2020, **103**: 3286–3298.
[51] Ritchie RO. The conflicts between strength and toughness. *Nat Mater* 2011, **10**: 817–822.
[52] Zhang C, Gupta A, Seal S, *et al.* Solid solution synthesis of tantalum carbide-hafnium carbide by spark plasma sintering. *J Am Ceram Soc* 2017, **100**: 1853–1862.
[53] Lawn B. *Fracture of Brittle Solids*. Cambridge: Cambridge University Press, 1993.
[54] Lipetzky P, Kreher W. Grain boundary toughness effects on crack propagation in brittle polycrystals. *Mater Sci Eng A* 1996, **205**: 110–116.
[55] Porz L, Wei S, Zhao JM, *et al.* Characterizing brittle fracture by modeling crack deflection angles from the microstructure. *J Am Ceram Soc* 2015, **98**: 3690–3698.
[56] Ni DW, Liu JX, Zhang GJ. Pressureless sintering of HfB_2–SiC ceramics doped with WC. *J Eur Ceram Soc* 2012, **32**: 3627–3635.
[57] Watanabe T, Tsurekawa S. Toughening of brittle materials by grain boundary engineering. *Mater Sci Eng A* 2004, **387–389**: 447–455.